PAPER • OPEN ACCESS

Beyond periodicity: tailoring Tamm resonances in plasmonic nanohole arrays for multimodal lasing

To cite this article: Shadman Shahid and Muhammad Anisuzzaman Talukder 2025 *New J. Phys.* **27** 013014

View the article online for updates and enhancements.

New Journal of Physics

The open access journal at the forefront of physics

PAPER

Beyond periodicity: tailoring Tamm resonances in plasmonic nanohole arrays for multimodal lasing

Shadman Shahid[1,2] and Muhammad Anisuzzaman Talukder[1,*]

[1] Department of Electrical and Electronic Engineering, Bangladesh University of Engineering and Technology, Dhaka 1205, Bangladesh
[2] Department of Computer Science and Engineering, BRAC University, Dhaka 1212, Bangladesh
[*] Author to whom any correspondence should be addressed.

E-mail: anis@eee.buet.ac.bd

Abstract

Extraordinary optical transmission (EOT) through metal nanohole arrays (NHAs) and Tamm plasmon (TP) states have been investigated in plasmonic devices since 1998 and 2007, respectively. Since their introduction, various potential applications for structures that support these phenomena have been reported, including plasmonic absorbers, lasing cavities, and narrowband filters. The performance of EOT- and TP-based devices is significantly influenced by the sizes and patterns of the holes in the NHA. While the effects of hole size and shape on EOT have been extensively studied, similar research on TP structures involving metal NHAs is still lacking. Particularly, the impact of gradually introducing randomness into the metal NHA on TP modes has yet to be explored. In this work, we modify the hole sizes and arrangements of the metal NHA and examine the effects on EOT and Tamm resonances. We investigate three scenarios: the bare metal NHA, a passive Tamm resonant cavity, and a TP laser. We observe that multiple Tamm resonances appear as the periodicity of the holes increases. However, these resonances vanish when the hole arrangement shifts from a regular array to a pseudo-periodic random array, which is defined as a collection of holes placed randomly within a periodically repeating square unit cell. These multiple resonances can be attributed to the folding of dispersion lines in a periodically patterned TP cavity. The dispersion characteristics of the NHA array-based structures are calculated and analyzed to understand better the multiple resonances in the transmission and lasing emission patterns.

1. Introduction

Uniform arrays of subwavelength holes etched onto a thin metal film enhance transmission through the film [1]. Since being first reported in 1998, much research has been conducted to study the effects of hole shapes, sizes, array periodicity, metal film thickness, and materials on the extraordinary optical transmission (EOT) characteristics through a metal nanohole array (NHA) [2–5]. When such a metal film with nanoholes is incorporated on top of a distributed Bragg reflector (DBR), Tamm plasmon (TP) states are observed at the metal–DBR interface [6–9]. The theoretical basis of the EOT phenomenon through metal NHAs [10–13] and TP resonances at the metal–DBR interface has been extensively studied [14–17]. Recently, significant research efforts have focused on engineering and utilizing TP states for various applications, such as photodetection [18, 19], absorption [20–22], photovoltaics [23], sensing [24, 25], and lasing [16, 26–29]. The TP spectrum can be tailored by modifying the DBR characteristics and the textures and patterns on the metal layer, such as discs [14–16, 30], strips [31–33], NHAs [26], and slits [34]. These structures can control TP resonances by altering the metal patterning, making them useful for various applications, including multimodal lasing [28] and nonlinear plasmonics [35].

The TP states in a structure with metal NHA are significantly different in physical footprint and behavior compared to the EOT resonances of the same structure. TP states show narrower linewidth than the EOT resonances. Thus, TP resonances' high Q-factors make them especially suitable as cavity modes in lasers in

contrast to the low Q-factor EOT resonances of a standalone metal NHA [17, 26, 36]. Recently, Ahmed and Talukder have numerically validated that plasmons are responsible for the lasing action in the metal NHA-based laser reported in [26], opening up new avenues to tailor and engineer novel spectral features in such devices [27, 37]. Modification of the lasing spectrum has been reported in such TP lasers (TPL) by modifying the metal NHA as well as the DBR [28, 38].

Recently, dual-mode plasmonic lasing has been reported from a TP cavity that merged two-fold periodicity in its NHA arrangement [28]. Such an arrangement of holes on the metal film has been termed a merged lattice (ML), derived from a similar concept proposed for two-dimensional (2D) photonic crystals [39]. The TP devices with a simple square periodic NHA on the metal layer exhibit single mode response and consequently single mode lasing emission from TPLs [26, 37]. However, the ML NHA pattern in the metal layer of the Tamm cavity results in a dual-mode resonance [28]. While the dual resonances in [28] occurs only weakly in the EOT spectrum for the standalone ML metal NHA; they are much more prominent in the TP cavity. Thus, TP resonances offer better quality modes for lasing than the EOT modes. Recently, Ferrier *et al* also reported a multi-resonant TP structure with one-dimensional patterning of metal strips on top of a DBR [31]. The structure formed a TP bandgap cavity with a dual-mode spectrum at normal incidence.

However, efforts are still needed to explore why multiple TP modes may arise from such patterning and arrangement of perforations in the metal layer. Additionally, no work has investigated the effects of complex hole arrangements, such as irregularity in the hole patterns, on TP resonances and lasing characteristics. A detailed and comprehensive study of the impact of the metal NHA's hole arrangements in TP devices would help design devices exhibiting diverse TP modes. While a metal film with ML NHA has been reported to elicit dual-wavelength resonance, the physics behind the dual mode emission from the TP lasing cavity is yet to be analyzed on a granular level. Different hole arrangement scenarios in metal NHA should also be investigated.

In this article, we investigate the nanohole arrangements on a thin gold (Au) film in a TP structure and demonstrate its potential for designing laser cavities. Dispersion and transmission characteristics of such devices are analyzed to understand their modal characteristics. We vary the configuration from a perfectly ordered square array to a randomly distributed set of nanoholes to investigate the effect of hole arrangement regularity in the Au-NHA. We model different strategies for placing holes in the Au film, encompassing a set of periodic, pseudo-periodic, and random nanoholes. The arrangement of holes within a unit cell is randomized based on a normal (Gaussian) or uniform distribution. This study focuses on how different hole sizes and arrangements affect the EOT characteristics in a bare Au-NHA and, subsequently, the plasmonic resonances of a TP cavity formed with the same Au-NHA. The identified TP cavity resonances are then applied in a plasmonic laser, where crucial lasing characteristics, such as the emission spectrum, lasing threshold, and far-field characteristics, are analyzed.

Our analysis and findings showcase the pivotal role of hole-to-hole periodicity, not just the spacing but the arrangement within a unit cell, in defining the plasmonic resonance characteristics of both standalone metal NHAs and TP cavities. In this regard, adjusting the hole sizes in relation to the unit cell period would also significantly optimize the lasing cavity modes. The gradual incorporation of disorder, especially through an ML arrangement, induces multiple resonances that display varied spectral and emission characteristics. However, the highest level of disorder with a completely random arrangement does not yield multiple resonances. This observation was consistent across normal and uniform random hole distributions. Dispersion analysis provided insights into resonance, mode coupling, confinement, and the slowness of light. Our comprehensive analysis concludes by proposing an optimized device configuration and identifying the optimal hole size for various TPL configurations.

2. Methodology

The multilayer TPL analyzed in this work can be decomposed into three key components: the Au-NHA layer, a DBR, and a layer of polyurethane (PU) that hosts the gain medium, as shown in figure 1. The Au-NHA with an undoped PU layer and the DBR constitute the passive TP cavity, designed to be resonant at the lasing wavelength of the gain medium, i.e. IR-140 dye molecules. The light-matter interactions in the passive cavity and the active laser device presented in this work have been simulated using a commercial finite difference time domain (FDTD) solver [40]. This investigation focused on dispersion analysis and the transmission and emission characteristics of the devices. The lasing threshold characteristics and the electric field profile of the TPL for different NHA schemes have also been investigated.

2.1. Structure description and parameterization
The devices analyzed and the direction of optical excitation are shown in figure 1. Figures 1(a) and (b) depict the TP cavity with a 100 nm-thick perforated Au film on top of a PU layer. The various hole arrangement schemes shown in figures 1(c)–(e) are applied to the Au layer on top of the TP resonant cavity in figure 1(b).
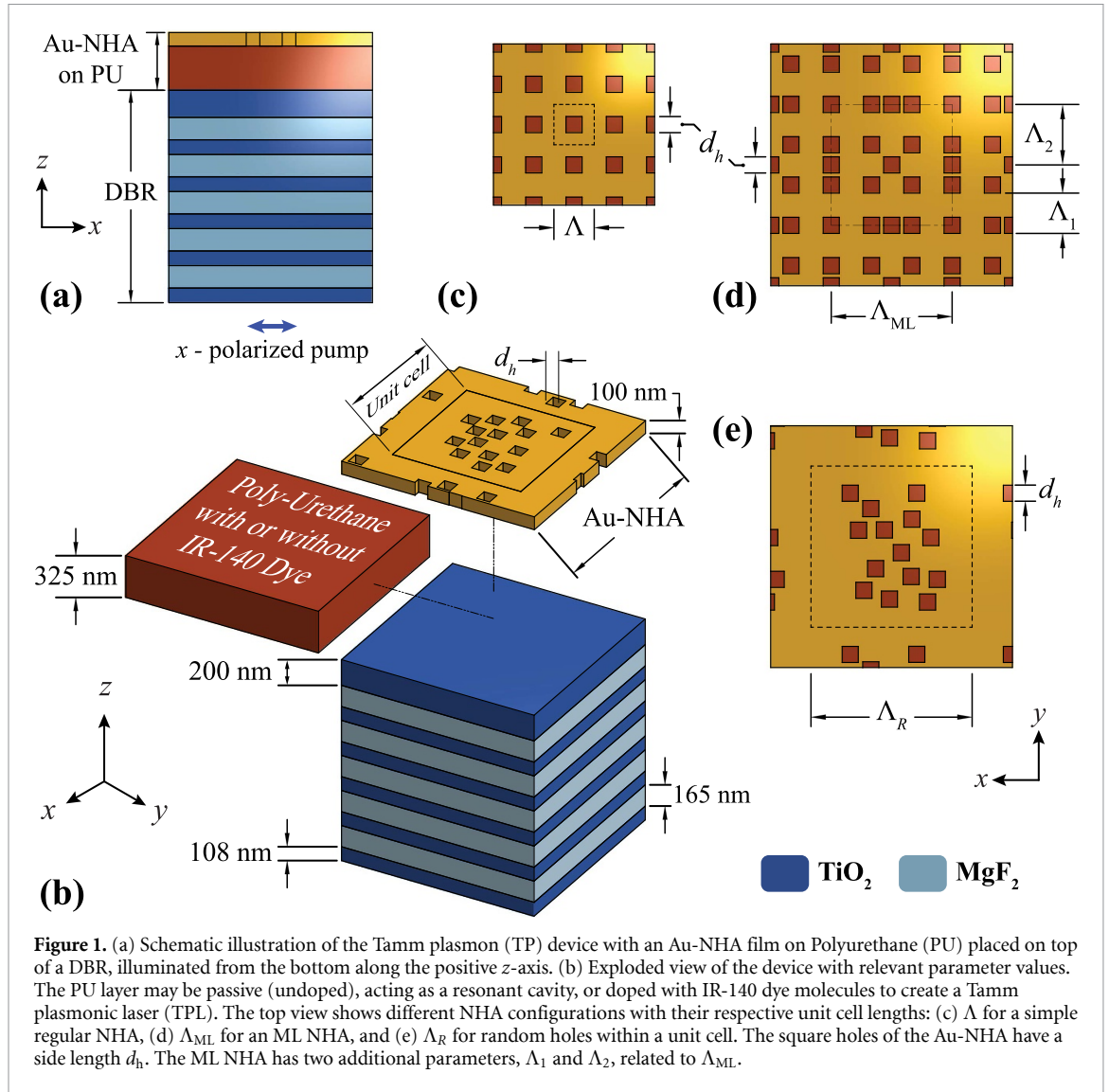
Figure 1. (a) Schematic illustration of the Tamm plasmon (TP) device with an Au-NHA film on Polyurethane (PU) placed on top of a DBR, illuminated from the bottom along the positive z-axis. (b) Exploded view of the device with relevant parameter values. The PU layer may be passive (undoped), acting as a resonant cavity, or doped with IR-140 dye molecules to create a Tamm plasmonic laser (TPL). The top view shows different NHA configurations with their respective unit cell lengths: (c) Λ for a simple regular NHA, (d) Λ_{ML} for an ML NHA, and (e) Λ_R for random holes within a unit cell. The square holes of the Au-NHA have a side length d_h. The ML NHA has two additional parameters, Λ_1 and Λ_2, related to Λ_{ML}.

When the PU layer is doped with IR-140 dye molecules, the passive device is transformed into an active device, i.e. a TPL, as shown in figure 1(b). The NHA features of the Au film are modified by adjusting the hole arrangement, unit cell length (Λ), and hole sizes (d_h). Figures 1(c)–(e) show three different hole arrangement schemes. The first scheme, shown in figure 1(a), is a simple periodic square array of square nanoholes with a periodicity of Λ. The next scheme in figure 1(d) depicts an ML configuration with two periodic square arrays of periodicities Λ_1 and Λ_2 placed concentrically [39]. Finally, figure 1(d) represents the scheme in which nanoholes are placed randomly in the Au film. In the ML scheme, the unit cell length (Λ_{ML}) is the lowest common integer multiple of Λ_1 and Λ_2. An integer parameter R relates Λ_{ML} to Λ_1 and Λ_2 as

$$R = \Lambda_{ML}/\Lambda_1 = \Lambda_{ML}/\Lambda_2 + 1, \tag{1a}$$

$$r = \Lambda_2/\Lambda_1. \tag{1b}$$

Equation (1a) limits Λ_1 and Λ_2 values to maintain a fixed ratio of r. The ML scheme represents a quasi-periodic state of hole arrangement that has a short-scale disorder. The level of disorder within the unit cell increases with R. In this work, we have simulated results for devices when $R = 3$, 4, and 5, with the unit cell lengths mentioned in table 1. Figures 2(a)–(c) show the top views of devices with ML NHAs from table 1, where $\Lambda_{ML} = 0.75$, 1.5, and 2.5 μm.

We introduce randomly placed nanoholes on the Au film to simulate increased irregularity in hole placement for both the standalone Au film and the Au film as part of the TP device, as shown in figure 1(e). Ideally, any planar feature considered random in a 2D plane should extend infinitely in both dimensions. Thus, the transverse dimensions over which they are applied should be increased to simulate random features accurately, bringing the simulation closer to ideal randomness and improving its accuracy. However, larger device dimensions result in longer simulation times and higher computational costs. Therefore, a trade-off

Table 1. Values of different parameters used in the simulation of the TP structure and the metal film patterning.

Au film pattern parameters (along x–y plane)			
Square hole side length		$d_h = 100\,\text{nm}$	
Simple periodic NHA (Unit cell period Λ)	Merged lattice (Unit cell period Λ_{ML})		Random lattice NHA (Unit Cell Period Λ_R)
$\Lambda = 250\,\text{nm}$	$R = 3$ $\Lambda_{ML} = 750\,\text{nm}$	$\Lambda_1 = 250\,\text{nm}$ $\Lambda_2 = 375\,\text{nm}$	Gaussian random distribution: $\Lambda_R = 1\,\mu\text{m}$
	$R = 4$ $\Lambda_{ML} = 1.5\,\mu\text{m}$	$\Lambda_1 = 375\,\text{nm}$ $\Lambda_2 = 500\,\text{nm}$	
$\Lambda = 375\,\text{nm}$	$R = 5$ $\Lambda_{ML} = 2.5\,\mu\text{m}$	$\Lambda_1 = 500\,\text{nm}$ $\Lambda_2 = 625\,\text{nm}$	Uniform Random distribution: $\Lambda_R = 1\,\mu\text{m}$
DBR and TP structure parameters (along z-axis)			
TiO$_2$ layer parameters		$d_1 = 109\,\text{nm}$	$n_1 = 2.23$ [6]
MgF$_2$ layer parameters		$d_2 = 165\,\text{nm}$	$n_2 = 1.46$ [6]
Final TiO$_2$ layer parameters		$d_L = 200\,\text{nm}$	$n_L = 2.23$ [6]
PU Spacer/Gain layer parameters		$d_S = 325\,\text{nm}$	$n_S = 1.51$ [41]
Au layer parameters		$t = 100\,\text{nm}$	$n_M = n_M(\lambda)$ [42]

Figure 2. ML NHA configuration and random hole ensemble arrangements. Three regimes of the ML NHA configuration given in table 1 are shown with (a) $\Lambda_{ML} = 750\,\text{nm}$, $R = 3$, $d_h = 143\,\text{nm}$; (b) $\Lambda_{ML} = 1.5\,\mu\text{m}$, $R = 4$, $d_h = 175\,\text{nm}$; and (c) $\Lambda_{ML} = 2.5\,\mu\text{m}$, $R = 5$, $d_h = 175\,\text{nm}$. Each regime has different Λ_1 and Λ_2 values as per equation (1a). (d)–(f) Normally distributed random nanoholes, and (g)–(i) uniformly distributed random nanoholes within a square unit cell of length $\Lambda_R = 1\,\mu\text{m}$ and $d_h = 100\,\text{nm}$.

must be made to balance acceptable accuracy with manageable time and computational costs. To address this trade-off, the transverse simulation domain and the device are made periodic with a unit cell dimension of Λ_R. The holes are placed randomly within each unit cell, a configuration we refer to as a pseudo-periodic random array. While this method of hole placement is not perfectly random, it exhibits greater randomness than the previously mentioned ML scheme. Similar to the ML approach, the degree of randomness can be increased by increasing the dimension of the unit cell Λ_R. We set $\Lambda_R = 1\,\mu\text{m}$ for our analysis.

Two types of random hole distributions—normal and uniform—are studied for in-depth analysis of the impact of the random hole arrangement in NHA. In a normal distribution of nanoholes, the density ρ_{nd} within a unit cell approximately follows a centered Gaussian function as

$$\rho_{nd} \propto \exp\left[-\left(x^2 + y^2\right)/\left(2\sigma^2\right)\right]. \tag{2}$$

Equation (2) expresses ρ_{nd} in terms of a Gaussian function, with x and y representing the distances along the transverse directions from the center of the device, and σ as the standard deviation of the distribution. In contrast, for a uniform distribution, the density $\rho_{ud} = 13 \sim 14\,\mu m^{-2}$ is nearly constant throughout the unit cell. figures 2(d)–(f) show arrangements of normally distributed holes along both transverse directions, while figures 2(g)–(i) display uniformly distributed holes within the unit cell, with a density of 13 to 14 square nanoholes per μm^2, each having a width of $d_h = 100$ nm. Since the nanohole size is only one-tenth of the unit cell length, the differences between the two distributions are subtle.

A perforated Au film on a PU substrate without DBR is analyzed first. PU is chosen as the substrate material for the standalone Au-NHA as PU is the host of the laser gain medium in this work. The substrate acts as a homogeneous medium from which the Au film can be optically excited. The second category consists of a passive TP structure, which is a multilayer dielectric stack consisting of a DBR and a PU spacer layer terminated by an Au-NHA film. The DBR consists of five alternating layers of TiO_2-MgF_2 followed by an additional terminating TiO_2 layer of 200 nm thickness. Alternating TiO_2 and MgF_2 layers in the DBR have 108 and 165 nm thicknesses, respectively. The PU spacer layer, which serves as a host medium for IR-140 dye molecules, has a thickness of 325 nm. In an active TPL, the PU layer is doped by IR-140 dye molecules. The necessary structural parameters of the simulated structures are presented in table 1.

2.2. Simulation

The dispersion and transmission characteristics of the passive device were analyzed using FDTD simulations. Dispersion analysis gives us the relation between the frequency (energy) and wavevector (momentum) of light waves through the structure, helping to determine a system's possible modes and the band structure. Transmission analysis, on the other hand, helps to identify the normally transmitted modes through a structure. Since the simulated structures are periodic on the xy plane, the rectangular region defined by the structure's unit cell is considered as the simulation region with Bloch or periodic boundary conditions (BCs). The Bloch BC differs from the periodic BC in applying the necessary phase change at the boundaries for oblique incidence. Bloch BCs were used in dispersion analysis as the frequency spectrum of the devices with input waves at different k-values, and hence directions, are required. Periodic BCs apply no phase change at boundaries and are appropriate for the transmission analysis where only the normal light incidence is considered. As the simulated devices are longitudinally aligned along the z axis, perfectly matched layer (PML) BCs are used at the boundaries normal to the z axis for absorbing the radiated waves. The nanoholes in the simulation region have a fixed mesh size of 5 nm along the x and y axes and 10 nm along the z axis. The rest of the simulation region has an adaptive non-uniform rectangular meshing based on the material index and the FDTD time step.

The dispersion analysis of passive structures involved many arbitrarily placed dipole sources within the FDTD simulation region. These sources excite the device's modes that are recorded by several randomly placed time domain monitors. The time domain data from the randomly placed monitors are Fourier transformed to get the frequency domain information of the resonant modes for different propagation vectors along the x-axis Bloch boundary (k_x). The E vs. k relation is plotted for a range of k_x from 0 to π/Λ. For the first category of structures, as shown in figures 1(a)–(e), the substrate beneath the 100-nm-thick metal film extends through the lower PML boundary in the z direction. The z-span of the simulation region has the PU substrate, followed by the Au-NHA, and then a layer of vacuum (or air). As only the wavevector along the x axis, i.e. k_x, is computed for the dispersion analysis, further simplifying the simulation region was possible by making the Bloch BCs symmetric along the y boundaries.

The second category of structures, shown in figure 1(f), exhibits the same Au-NHA film in a TP structure. Due to the addition of the DBR, the simulation region is elongated along the z axis. The transverse dimensions and boundaries remain unchanged. In this case, the symmetric boundary simplification also holds as only k_x is evaluated. The BCs at the transverse boundaries are set to periodic for transmission analysis since only normal near-field transmission is required. The normal transmission spectra presented are excited by a broadband plane wave source normal to the transverse plane of the structures given in figure 1. The plane wave source is placed at least $\lambda_{max}/2$ distance away from the device in the air (vacuum), opposite to the Au-NHA end of the device, where λ_{max} is the upper limit of the wavelength range of the broadband source. Placing the source at such distances away from the device ensures that the wavelengths in the broadband source reach the device without being diffracted away. Near-field transmission data is obtained from a 2D plane located 1 μm in front of the structure on the transmission side.
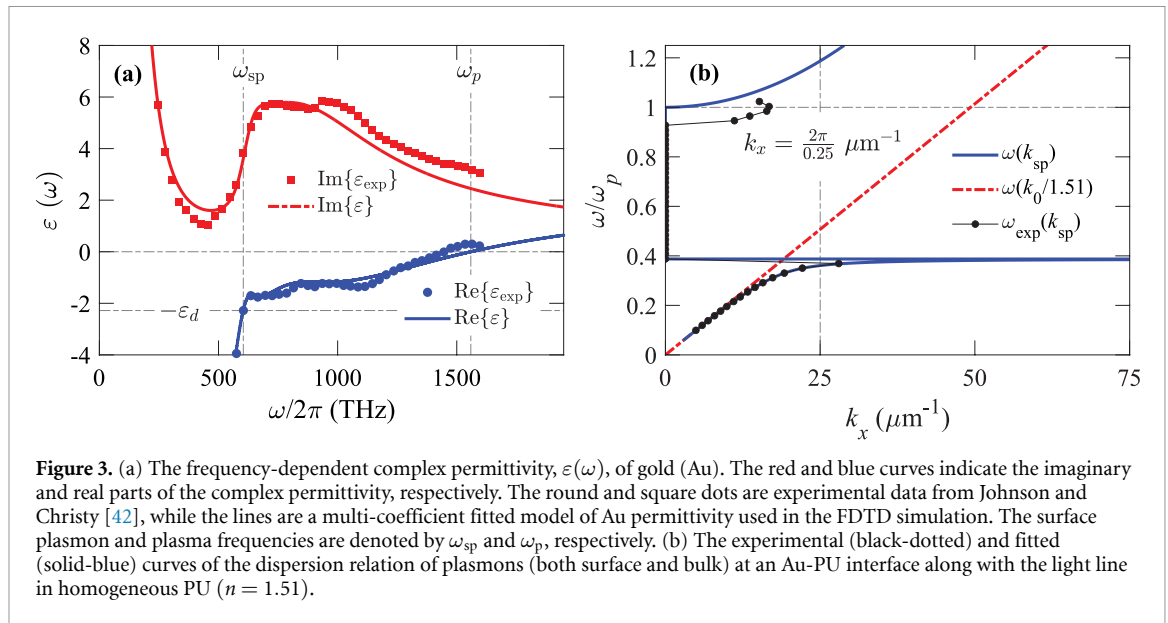
Figure 3. (a) The frequency-dependent complex permittivity, $\varepsilon(\omega)$, of gold (Au). The red and blue curves indicate the imaginary and real parts of the complex permittivity, respectively. The round and square dots are experimental data from Johnson and Christy [42], while the lines are a multi-coefficient fitted model of Au permittivity used in the FDTD simulation. The surface plasmon and plasma frequencies are denoted by ω_{sp} and ω_p, respectively. (b) The experimental (black-dotted) and fitted (solid-blue) curves of the dispersion relation of plasmons (both surface and bulk) at an Au-PU interface along with the light line in homogeneous PU ($n = 1.51$).

2.3. Material modeling

Except for Au in the Au-NHA film and the IR-140 dye gain medium, other materials in this work, such as TiO_2, MgF_2, and PU, are modeled as homogeneous and non-dispersive media. TiO_2, MgF_2, and PU have indices of 2.23, 1.46, and 1.51, respectively [6, 43]. Au was the metal of choice because of its superior plasmonic features compared to copper or silver [44, 45]. Analytical permittivity models of Au, such as the Drude–Lorentz model, often cause gross simplification in the calculation, resulting in a significant discrepancy between simulation and experimentally reported results. Therefore, the frequency-dependent permittivity, $\varepsilon(\omega)$, of Au is modeled after the experimental values obtained from Johnson and Christy, as shown by the discrete dots in figure 3(a) [42].

IR-140 dye molecules in the PU host are the gain medium in the active laser structure. The gain medium has been modeled as a semi-classical four-level two-electron system coupled to Maxwell's equations solved using the FDTD method [46]. The parameters of the four-level two-electron model were obtained from [43]. The gain medium has dye molecules that absorb light at 800 nm and emit at 870 nm. Thus, in our analysis, the TPL is pumped by a plane wave source of 800 nm wavelength with 40 fs pulse duration. Since the laser has a gain linewidth of 100 nm, the laser supports cavity modes in the 820–920 nm wavelength range. The modes within this range are amplified by the Gaussian gain lineshape of IR-140 dye and transmitted through the structure with gain.

3. Results and discussion

In this section, we present and discuss the impact of hole sizes and arrangements on the device functionality of three different categories of structures. The first category consists of an Au-NHA on a PU substrate. Next, we discuss passive TP cavities incorporating the Au-NHA. The final category comprises plasmonic lasers with lasing cavities formed using the TP cavity structure. Our analysis reveals an optimized square nanohole size and the ability to engineer multimode emission using different NHA configurations. However, multimodal characteristics in the spectrum emerge only for specific hole configurations.

3.1. Category 1: Au-NHA on PU substrate
3.1.1. Effect of hole size
The Au-NHA on the PU substrate is analyzed to observe the effect of regular, quasi-regular, and periodically random arrangement of holes in the NHA. The critical figure of merit for EOT is the transmission relative to the open hole fraction of the Au-NHA, which is the normalized transmission (T_{norm}). T_{norm} exceeds the prediction of the Bethe–Bouwkamp power model ($T \propto d_h^4$) for the smaller holes [47] but saturates for larger holes. T_{norm} also exhibits a slight blueshift with an increasing linewidth. The optimum range of d_h for different Λ is determined by observing variations of the EOT spectrum. Furthermore, the dispersion relation of the Au-NHA for different Λ characterizes the change of spectrum properties with the variation of the hole arrangement.
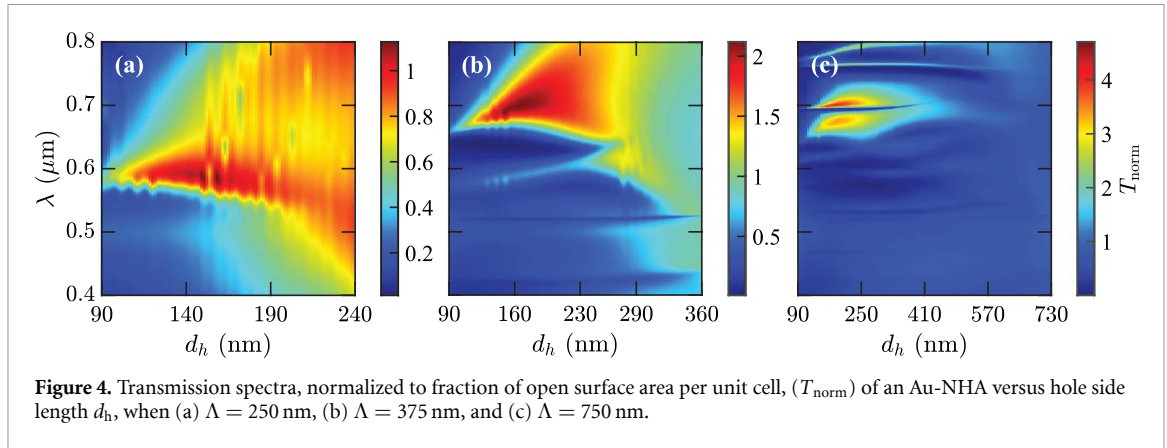
Figure 4. Transmission spectra, normalized to fraction of open surface area per unit cell, (T_{norm}) of an Au-NHA versus hole side length d_h, when (a) $\Lambda = 250$ nm, (b) $\Lambda = 375$ nm, and (c) $\Lambda = 750$ nm.

The transmission spectrum for varying d_h of an Au-NHA is shown in figure 4 for different Λ values. Increasing hole dimension causes the transmission mode linewidth to increase and, consequently, the Q-factor to decrease. As the spectrum is normalized to the fraction of hole area per unit cell, the normalized transmission changes for different values of Λ. The smallest Λ of 250 nm results in a transmission peak at $\sim$587 nm. With increasing d_h, the resonance linewidth increases, and the transmission peak experiences a blue shift of $\sim$3 nm. For the entire range of d_h, the transmission spectrum in figure 4(a) shows a single resonance only.

In contrast, figure 4(b) shows dual resonances for an Au-NHA when $\Lambda = 375$ nm and $d_h \leqslant 245$ nm, although one resonance is weaker. However, these dual resonances merge for $d_h > 245$ nm, creating a weak but broadband transmission. Further complexity in the transmission peaks is observed when $\Lambda = 750$ nm where at least three modes are observed in the spectrum in figure 4(c). This spectrum shows the highest transmission relative to the open surface area of the Au-NHA. For each value of Λ, a range of d_h results in the maximum possible transmission relative to the area of the hole. In the following dispersion analysis of Au-NHA with different Λ values, a d_h value within this optimal range is selected for each period.

3.1.2. Dispersion analysis
The transmission spectra of figure 4 are maximized at d_h values of 143 nm, 176 nm, and 200 nm for Λ values of 250 nm, 375 nm, and 750 nm, respectively. We perform a dispersion analysis of the Au-NHAs to understand the trade-off between larger transverse dimensions and the appearance of multimode transmission associated with a greater Λ in the Au-NHA for these specific hole sizes. The dispersion of Au-NHA on a PU substrate is compared with the theoretical dispersion calculations based on the Drude–Lorentz model for Au.

Simple periodic NHA
Subwavelength holes or apertures-both singular and arrays-etched onto thin metallic films exhibit surface plasmon polariton (SPP) and localized surface plasmon resonances [3, 11, 12]. Theoretical models of EOT through a metal NHA based on SPPs provide accurate explanations of the underlying mechanisms and successfully predict conditions for enhanced transmission [12, 48]. The SPP wavevector $\vec{k}_{spp} = k_0 \sqrt{\epsilon_d \epsilon(\omega)/[\epsilon_d + \epsilon(\omega)]}$ and the SPP resonance at a smooth Au–PU interface depend on the PU substrate's index, $n = \sqrt{\varepsilon_d} = 1.51$, and the Au film's permittivity, $\varepsilon(\omega)$. Here, $k_0 = \omega/c$ represents the free space wavevector of radiation. Figure 3(b) shows the SPP dispersion relation at an Au–PU interface, where the permittivities are obtained from the experimental values in [42] (black-dotted curve) and from the fitted FDTD material model (solid blue curve).

In figure 3, $\vec{k}_{spp}$ is greater than the wavevector in PU, $\vec{k_0}/1.51$, for any $\omega > 0$. Therefore, some additional mechanisms must provide extra momentum to the incident photons. Periodic patterns, such as subwavelength hole arrays on metal films, can provide the necessary in-plane wavevector to excite SPPs through the NHA's additional reciprocal lattice vector components along the two transverse axes. This phenomenon can be observed in figure 5 from the dispersion relation of the periodically patterned metal film. The $\vec{k}_{spp}$ in a metal film with a simple periodic 2D pattern having reciprocal lattice vectors $\vec{G}_x$ and $\vec{G}_y$ is given by

$$\vec{k}_{spp} = \vec{k}_x \pm i\vec{G}_x \pm j\vec{G}_y, \tag{3a}$$

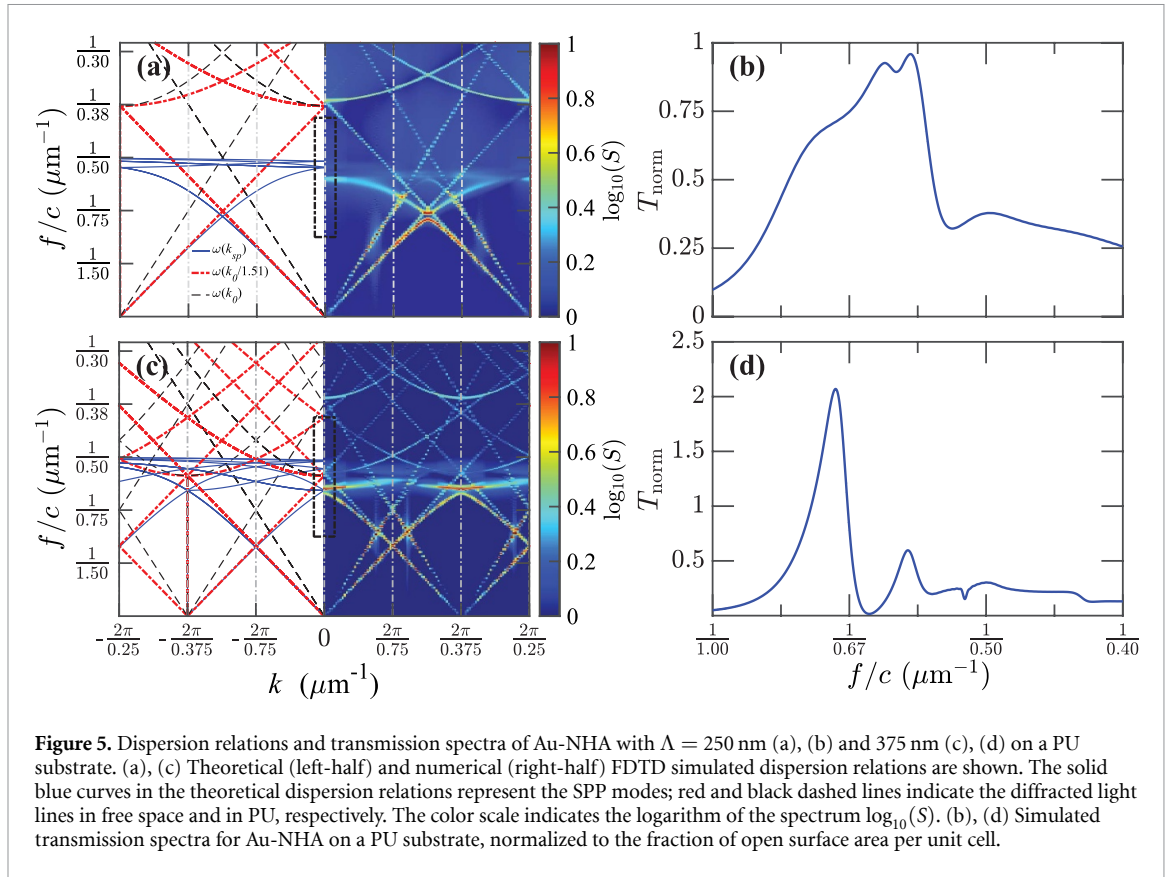$$\vec{G}_{x,y} = \frac{2\pi}{\Lambda_{x,y}}. \tag{3b}$$

Figure 5. Dispersion relations and transmission spectra of Au-NHA with $\Lambda = 250$ nm (a), (b) and 375 nm (c), (d) on a PU substrate. (a), (c) Theoretical (left-half) and numerical (right-half) FDTD simulated dispersion relations are shown. The solid blue curves in the theoretical dispersion relations represent the SPP modes; red and black dashed lines indicate the diffracted light lines in free space and in PU, respectively. The color scale indicates the logarithm of the spectrum $\log_{10}(S)$. (b), (d) Simulated transmission spectra for Au-NHA on a PU substrate, normalized to the fraction of open surface area per unit cell.

Here, $\vec{k}_x$ is the transverse x-component of the incident wavevector along the metal-dielectric interface, and $\omega/c = k_0$ is the free space wavevector (light line). The pair of integers (i,j) denotes the order of the reciprocal lattice. The reciprocal lattice vectors are inversely related to the pattern period $\Lambda_{x,y} = \Lambda$, i.e. the hole-to-hole period for an NHA pattern. The general dispersion relation for an Au film with an ordered NHA can be computed theoretically by solving equation (3) [48, 49]. The dispersion relations, i.e. ω vs. k relations, for the Au-NHA with $\Lambda = 250$ and 375 nm are shown in figures 5(a) and (b), respectively. The analytically calculated dispersion relationship is given in the left half of each plot, while the FDTD simulation is shown in the right half.

Due to the periodicity of the pattern, there is an infolding of the unpatterned Au film dispersion relation for every $2\pi/0.25 \, \mu\text{m}^{-1}$ in figure 5(a) and $2\pi/0.375 \, \mu\text{m}^{-1}$ in figure 5(b). This repetition corresponds to the Brillouin zone boundaries, beyond which the dispersion relation repeats for every $2\pi/\Lambda$ value. Also, because of the diffraction effect of the NHA on the Au film, the light line shows infolding just like that of the SPP modes. Thus, periodic patterning makes normal excitation of surface plasmon modes and photonic free space modes along the transverse plane possible, as the infolded modes intersect the $k_x = 0$ line at multiple points. Theoretically, solving equation (3) for normal incidence of light, i.e. $\vec{k}_x = 0$, gives us equation (4) by which the SPP resonant modes (λ_{spp}) in a metal NHA lattice can be obtained [50]

$$\lambda_{\text{spp}}(i,j) = \frac{a_0}{\sqrt{i^2 + j^2}}\sqrt{\frac{\epsilon_d \epsilon(\omega)}{\epsilon_d + \epsilon(\omega)}}. \tag{4}$$

When Λ increases from 250 to 375 nm, the reduced Brillouin zone in the ω-k diagram reduces, as observed in figure 5(b). Consequently, the density of modes at $k_x = 0$ is comparatively higher in figure 5(b) than in figure 5(a). The FDTD simulation results in figure 5 match the theoretical results except for the mode crossings at $k_x = 0$ and $2\pi/\Lambda$, which are avoided and create bandgaps [51]. These avoided mode crossings cause the dispersion modes from the FDTD simulation to occur at slightly lower frequencies than the theoretically predicted modes. We conclude that normally excited modes will resonate at lower frequencies (or higher wavelengths) with a greater unit cell length of the metal NHA, as evident in the dispersion
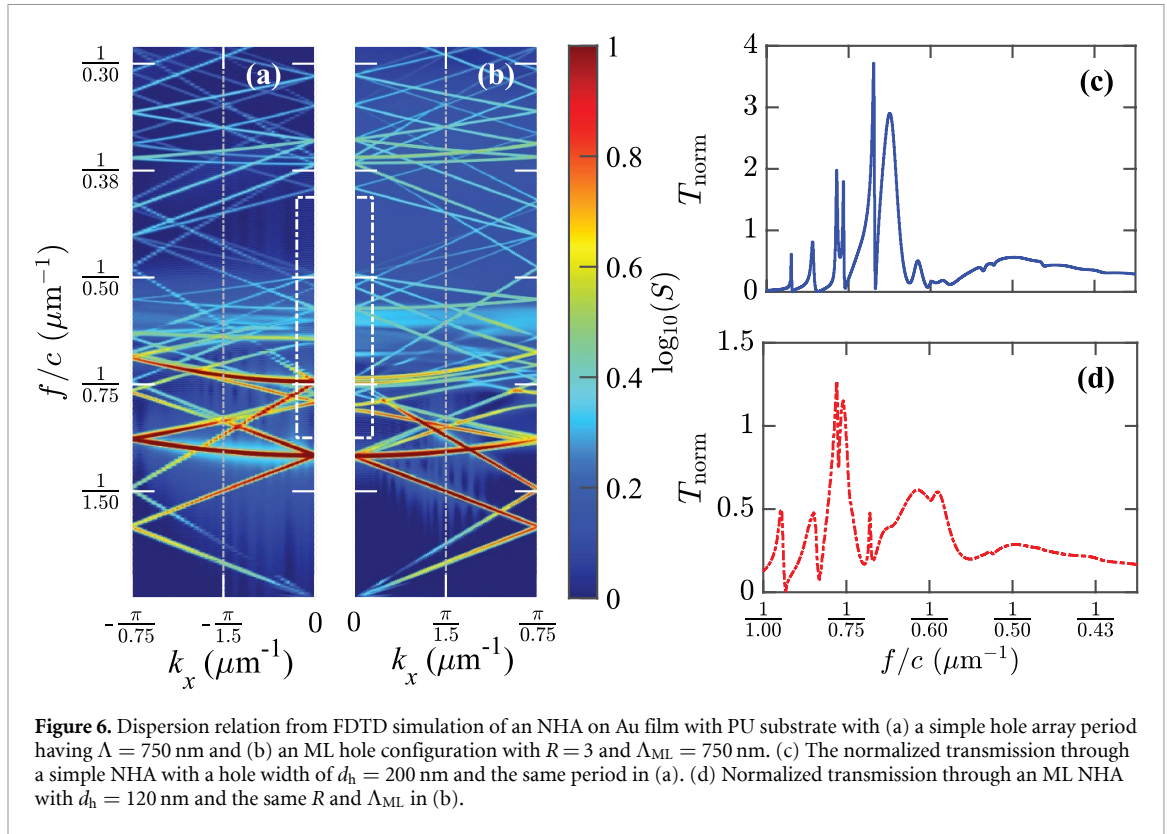
Figure 6. Dispersion relation from FDTD simulation of an NHA on Au film with PU substrate with (a) a simple hole array period having $\Lambda = 750$ nm and (b) an ML hole configuration with $R = 3$ and $\Lambda_{\text{ML}} = 750$ nm. (c) The normalized transmission through a simple NHA with a hole width of $d_{\text{h}} = 200$ nm and the same period in (a). (d) Normalized transmission through an ML NHA with $d_{\text{h}} = 120$ nm and the same R and Λ_{ML} in (b).

diagram of the metal NHA in figure 5, where Λ increases to 750 nm. Thus, the optimal d_{h} and the larger Λ in metal NHAs help to achieve multiple resonances due to the higher density of photonic states.
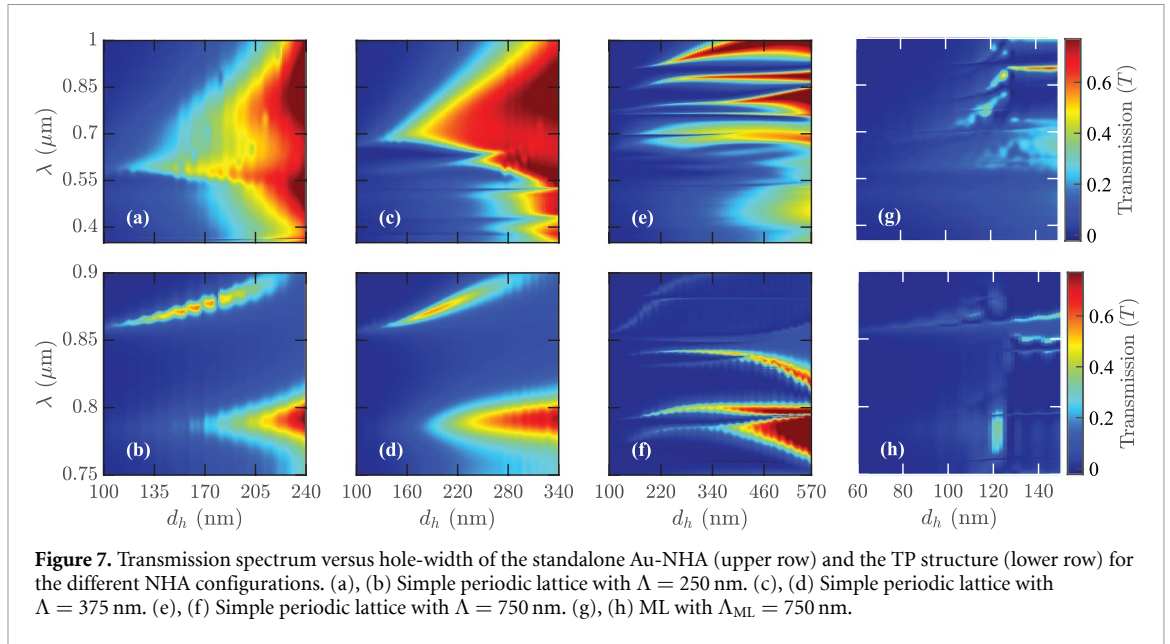
ML and Random NHA

The SPP modes in an Au film with an ML NHA ($R = 3$, $\Lambda_{\text{ML}} = 750$ nm) differ subtly from those of a simple NHA with $\Lambda = 750$ nm, as shown in figures 6(a) and (b). In particular, the ML NHA demonstrates greater splitting in the modes excited by normally incident beams ($k_x = 0$) than the simple periodic Au-NHA. The mode splitting is prominent for wavelengths between 0.7 and 0.85 μm. However, finer mode splitting can also be observed at other frequencies. The zeroth-order transmission spectra of the simple and ML NHA are shown in figures 6(c) and (d), respectively. Figure 6(c) shows that a simple NHA with $\Lambda = 750$ nm has multiple narrower and more intense resonances than its ML counterpart in figure 6(d). These multiple resonances exhibit band gaps in their spectrum. For both lattices, the d_{h} values are selected to maximize overall transmission, and both reveal multiple modes in the 0.4–1 μm wavelength range. The multimode resonances in the transmission spectrum of figure 6(d) extend from 0.6 to 0.75 μm and are broader than the modes in figure 6(c). Equal energy states under a simple 750 nm NHA exhibit greater splitting in the ML NHA. Thus, quasiperiodic ML structures facilitate multimodal transmission and tunable bandgaps.

For $R > 3$, the distribution of normally excited modes becomes denser than that for $R \leqslant 3$. The multiple closely spaced modes can fuse and create a broadband resonance. In addition, the bands for higher values of Λ_{ML} will be flatter at $k_x = 0$ due to a smaller Brillouin zone in the dispersion relation. These flatter bands result in better localization of the modes. However, for higher R values, the open-hole fraction of Au-NHA decreases, leading to attenuated transmission. The hole sizes can be increased to counteract this attenuation. However, increasing d_{h} in an ML causes hole overlaps if $d_{\text{h}} \geqslant \Lambda_1 / 2$. Despite the hole overlaps within the unit cell, the Au-NHA dispersion relation remains unchanged as the unit cell length remains unchanged. This hole overlap design preserves the characteristics of NHA-based TP devices.

Although a perfectly periodic NHA features a uniform hole arrangement, the disorder in the ML hole array increases with R. Continuing this trend, a design that further increases the level of disorder in the Au-NHA incorporates an entirely random hole arrangement in the Au-NHA. However, since a set of randomly positioned holes is periodically repeated, it is not perfectly random but rather an approximation of the ideal randomness.

Random placement of nanoholes on the Au film can result in significantly damped transmission. In such a case, the resonant transmission peak becomes ineffective as the transmission is negligible and unsatisfactory. The transmission spectrum resulting from the random positioning of square nanoholes in the

Figure 7. Transmission spectrum versus hole-width of the standalone Au-NHA (upper row) and the TP structure (lower row) for the different NHA configurations. (a), (b) Simple periodic lattice with $\Lambda = 250$ nm. (c), (d) Simple periodic lattice with $\Lambda = 375$ nm. (e), (f) Simple periodic lattice with $\Lambda = 750$ nm. (g), (h) ML with $\Lambda_{ML} = 750$ nm.

metal film adheres to the Bethe–Bouwkamp law, where $T \propto \lambda^{-4}$, showing no variation in transmission modes with the incidence angle and thus the in-plane wavevector, k_x. Thus, the transmission spectrum of a random set of square nanoholes on an Au-NHA does not offer novel or notable features for our cavity design, as no EOT phenomenon is observed [3]. However, the transmission spectrum can be narrowed and improved further when the Au film with the PU is coupled to a DBR in a TP structure. The effect of such random hole placement is novel and significant in the context of TP structures where Au-NHA acts as the top layer on the DBR. Figure 7 shows comparisons of the line widths and Q-factors of the transmission modes due to EOT with those of the TP cavity, highlighting superior performance in the TP cavities.

3.2. Category 2: TP structures

In the analyzed TP cavity, DBR acts as a dielectric mirror with a transmission band gap defined by the thicknesses and refractive indices of the TiO_2 and MgF_2 layers. The TP modes arise at the metal-DBR interface and remain within the constituent DBR bandgap. Imprinting patterns, such as strips or hole arrays on the metal film, can alter the TP modes' spectral positions but within the wavelength range of the constituent DBR's bandgap. With a variation of the controlling design parameters, the TP mode's wavelength can be tuned to anywhere within the bandgap. However, the TP modes at the bandedge have the best characteristics for lasing, such as high field enhancement and slow decay time [41]. The TP modes are significantly different from the EOT modes observed previously from the transmission spectrum of a standalone Au-NHA on a PU substrate.

Figure 7 presents the transmission vs. d_h plots of standalone Au-NHAs on PU substrate for different Λ values and the corresponding transmission spectra of TP cavities with an Au-NHA. Unlike the transmission spectrum in figure 4, normalized to the open-hole fraction of the NHA, figure 7 presents the absolute transmission through the analyzed devices. The plots in the upper row of figure 7 show that higher d_h values gradually broaden the EOT resonant modes. However, the transmission attenuates with a gradual decrease in the value of d_h, and multiple resonances emerge before converging to a single resonant wavelength of $\sim$600 nm for $d_h \rightarrow 0$. Nanostructuring the TP cavity—from an unpatterned Au layer to an ML configuration of holes—causes a slight redshift due to the coupling of additional modes introduced by the periodicity of the Au pattern. The transmission spectrum of the TP cavity with the ML configuration, the reflection spectrum of the unpatterned TP cavity, and the band gap of the constituent DBR are shown in figure S1. The splitting of the transmission spectra for intermediate d_h values is prominent for NHAs with greater Λ values.

However, the modes in TP structures with an Au-NHA are visibly different from those observed for the EOT spectrum with the same Au-NHA, i.e. the plots along the same column are significantly different. TP modes in the bottom row of figure 7 exhibit higher Q-factors than the EOT modes, and they are also shifted to a wavelength within the DBR bandgap. Thus, the high Q-factor of the TP modes, i.e. a narrow linewidth, makes them more suitable cavity modes than the EOT resonances. The plots in the first three columns are from devices with a simple NHA with a unit cell length of Λ, and the plots in the right column are from devices having an ML scheme with Λ_{ML}. Furthermore, in the bottom row of figure 7, when $d_h \rightarrow 0$, the TP cavity mode approaches $\sim$857 nm regardless of the value Λ. With an increasing d_h, the TP resonances exhibit

mode broadening along with a redshift. The broadening of the TP modes is much smaller than that of the EOT modes in the top row of figure 7.

The TP transmission spectrum shows the appearance of the lower bandedge of the constituent DBR bandgap at around ~800 nm for the highest d_h values in the transmission spectra of the plots in the bottom row of figure 7. At this maximum d_h in each of the bottom row plots of figure 7, the transmission is almost negligible above 800 nm, indicating a transmission bandgap. Furthermore, the TP mode remains within the DBR bandgap irrespective of d_h values. The TP modes for $\Lambda = 250$ and 375 nm occur at almost similar wavelengths, regardless of d_h. However, the $\Lambda = 750$ nm transmission spectrum in figures 7(e) and (f) shows multiple resonances for intermediate d_h values. From the TP transmission spectra, it is clear that the left edge (i.e. $d_h \to 0$) of the transmission versus d_h plot can be extrapolated to obtain the Tamm resonance of a TP cavity with an unpatterned Au layer. However, the spectra from the right edge of the plot, as mentioned earlier (i.e. $d_h \geqslant \Lambda$), will give us the DBR's approximate transmission bandgap spectra. However, TP resonances occur at different wavelengths within the DBR bandgap. TP cavities are not purely transmissive devices. Their reflection spectra, as shown in figure S2, exhibit similar features to those observed in the transmission spectra. An unpatterned TP cavity or cavities with $\Lambda = 250$ nm and $\Lambda = 375$ nm show a single cavity resonance, while the $\Lambda = 750$ nm configuration exhibits multiple reflection dips. In ML configurations, these multiple resonances overlap, creating a broad reflection dip, unlike the distinct narrow modes of the simple $\Lambda = 750$ nm case.
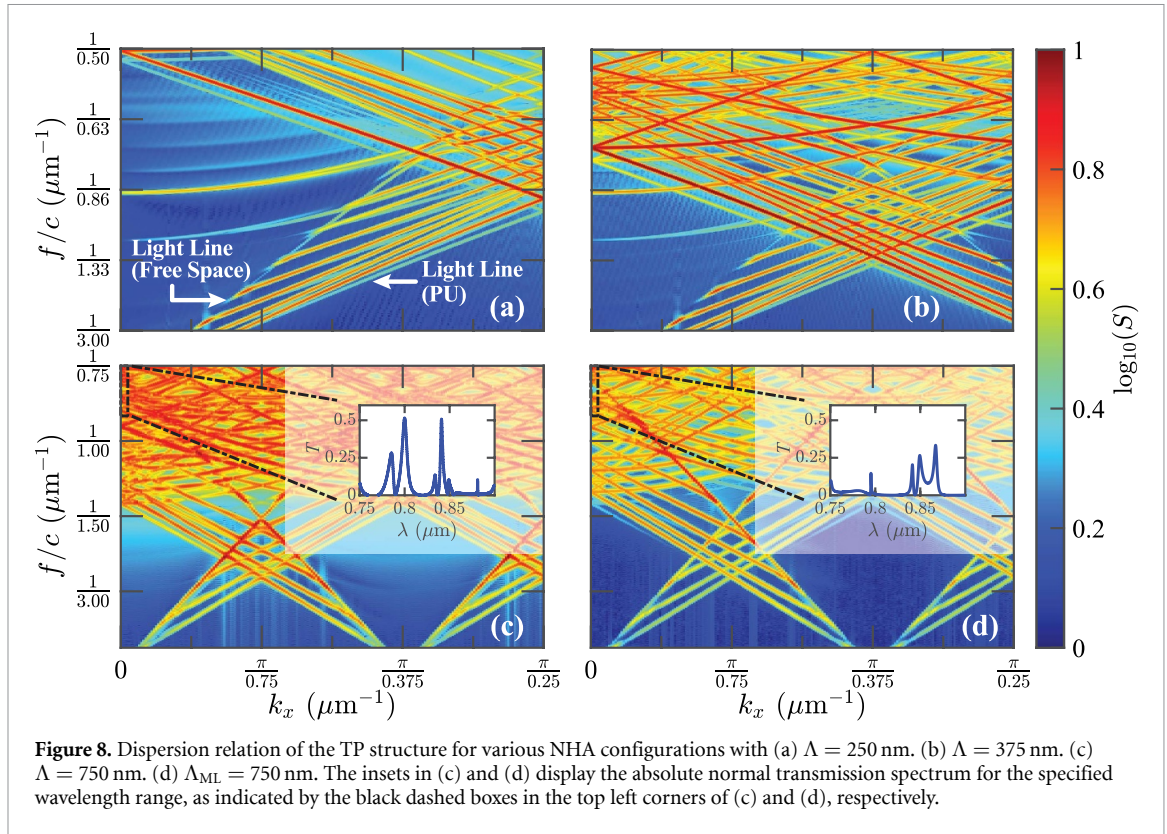
Figure 7(g) and (h) are the spectra of devices with an ML configuration with $\Lambda_{ML} = 750$ nm and $R = 3$. Dual-mode transmission with clear mode separation and narrow linewidths can be observed. For $R > 3$, multiple new modes appear in addition to the singular TP mode observed in figures 7(b) and (d), but they are comparatively more noisy and attenuated. The origin of these multiple noisy modes can be explained by analyzing the dispersion curves of the TP structure. The resonance wavelength of the EOT modes in an Au-NHA shifts due to changes in the effective refractive index of the adjacent medium. The change from a PU substrate to a DBR leads to higher quality resonances in the TP cavity, as shown in the bottom row of figure 7.

For photons and TPs in a TP cavity with an array of holes on the Au layer, the dispersion (*E-k*) diagram (or equivalently, frequency f versus wavevector k_x) shows periodic repetition, similar to the behavior in solid-state systems with electrons. The photon energy $E = hf$ is related to the frequency. Beyond the first Brillouin zone, the dispersion relation repeats, causing the dispersion lines to fold onto themselves. This results in dispersion lines from higher Brillouin zones appearing within the first zone, similar to a reflection off the zone boundary [31, 49].

Figure 8 shows the dispersion relations for TP structures with simple and ML NHAs, showing similarities to the EOT dispersion observed in figure 5. In these diagrams, multiple diffracted modes arise from the Au-NHA film. The multiple light lines observed between the light line in free space and that in PU represent the photonic modes introduced by the presence of the DBR. Figure 8(a) illustrates the first Brillouin zone of the TP structure with a lattice constant of $\Lambda = 250$ nm, which repeats periodically every $2\pi/\Lambda$ due to the periodic hole arrangement. This periodic repetition causes the dispersion lines at the Brillouin zone boundaries to be reflected into the first Brillouin zone, leading to the infolding of dispersion lines. For $\Lambda = 250$ nm, the TP mode around 870 nm is identified as the dominant mode in figure 8(a). Similarly, for $\Lambda = 375$ nm, the TP mode remains evident in figure 8(b). In figure 8(a), for the given frequency range, no diffracted modes are observed at $k_x = 0$. However, when Λ increases from 250 to 375 nm, the boundary of the Brillouin zone shifts to $\pi/0.375\,\mu m^{-1}$, leading to additional dispersion lines infolding from the edge of the Brillouin zone. This infolding is due to the periodicity of the Brillouin zone repetition, which now occurs every $2\pi/0.375\,\mu m^{-1}$, instead of every $2\pi/0.25\,\mu m^{-1}$. As a result, for $\Lambda = 375$ nm in figure 8(b), multiple resonances become available at $k_x = 0$ for $f/c \gtrsim 1/0.8\,\mu m^{-1}$, which are otherwise absent in figure 8(a).

Consequently, when $\Lambda = \Lambda_{ML} = 750$ nm, the diffracted modes arise at low enough frequencies around the TP mode at normal incidence, resulting in the TP mode to get lost within the many diffracted modes arising due to higher periodicity. These diffracted modes, which couple to the pure TP mode, appear as additional modes. Furthermore, in figure 8(d) for $\Lambda_{ML} = 750$ nm, there is more pronounced coupling and clearer band splitting at $k_x = 0$. Thus, with higher values of Λ, Λ_{ML}, and R, the increased periodicity in the NHA leads to denser multimode emissions by positioning the high photonic density of states within the desired wavelength range. However, the overlap between adjacent modes causes multiple modes to merge, forming a broader resonance with a lower Q-factor. The option Λ_{ML} is advantageous, as it further splits the fused modes. Therefore, using ML NHA on the Au film is better for maintaining multiple narrowband resonances with adequate transmission.

We observe that increasing the hole-to-hole period allows multiple resonances to become accessible at lower frequencies due to the infolding of dispersion lines at smaller k_x values, which enables previously inaccessible modes in the device to be utilized through periodic patterning. Randomness is introduced

Figure 8. Dispersion relation of the TP structure for various NHA configurations with (a) $\Lambda = 250$ nm. (b) $\Lambda = 375$ nm. (c) $\Lambda = 750$ nm. (d) $\Lambda_{ML} = 750$ nm. The insets in (c) and (d) display the absolute normal transmission spectrum for the specified wavelength range, as indicated by the black dashed boxes in the top left corners of (c) and (d), respectively.

through the ML configuration, where the degree of randomness is quantified by Λ_{ML}, representing the periodicity within which two arrays of different lattice constants (Λ_1 and Λ_2) are combined. A larger Λ_{ML} corresponds to a greater disparity between Λ_1 and Λ_2, which in turn increases the degree of randomness. However, the relationship between randomness and the number or spacing of resonances is not straightforward. The modes contributing to multiple resonances often vary significantly in peak transmission intensities. As a result, there is no universal criterion for quantitative optimization of the ML configuration to introduce randomness into the Au layer of the TP cavity.

In this work, we have resorted to dispersion and transmission spectrum analyses of the devices. For larger Λ values, the density of photonic states around the lasing frequency is higher compared to other frequencies, and the dispersion lines become flatter in the Λ_{ML} ML configuration. For these reasons, the dispersion lines at higher frequencies, in figures 8(c) and (d), become highly entangled at the $k_x = 0$ line, where lines from multiple Brillouin zones intersect. Additionally, as randomness increases, the phase relationships between modes can become incoherent because of random oscillations. This incoherence can suppress modes that are out of phase. Therefore, in an entirely random system, where holes are randomly distributed over an infinite expanse, multiple resonances are still inaccessible across all frequencies. This phenomenon is presented and elaborated on in the next section.

3.3. Category 3: TPL structure

When the PU layer in the TP structure is doped with IR-140 gain molecules, a TPL is formed. The field profile of the passive TP cavity under plane wave excitation shows how the device confines and intensifies the electric field, leading to laser action in the active device. With increasing Λ, the electric field enhancement increases. The rows of figure 9 show transmission spectra, transverse electric field profiles, and near-field lasing emission respectively from TP devices with simple periodic NHA when $\Lambda = 250$, 375, and 750 nm. Table 2 presents the optimal choice of d_h, which maximizes the field enhancement for each configuration. The first column in figure 9 shows the transmission spectra through the device with and without the IR-140 gain medium. The solid blue lines indicate the total transmission through the passive device, showing only a single resonance peak close to 870 nm for $\Lambda = 250$ and 375 nm. However, when $\Lambda = 750$ nm, the band infolding and multimode generation result in a multimode transmission spectrum. Notably, the slight redshift observed in the lasing mode in the red-dotted lasing emission curve of the first column results from mode detuning caused by the active IR-140 dye medium.

In figure 9, the transverse electric field profile at the Au–PU junction in the passive TP structure shows different enhancement levels for three Λ values. The maximum enhancement is 14.4 times, with

Figure 9. Characterization of passive and active(-lasing) TP cavities with various configurations of simple (non-merged) NHAs. First column (a), (d), (g): transmission spectra of the passive Tamm structure, depicted by the blue curve, and the lasing emission curve, depicted by the red curve for NHAs with different period lengths. Second column (b), (e), (h): transverse electric field profiles at the Au-PU interface within the passive TP cavity at its highest resonant mode. Third column (c), (f), (i): near-field lasing emission profiles of the TPL for the corresponding period lengths. The three rows represent NHAs with period lengths of (a)–(c) 250 nm, (d)–(f) 375 nm, and (g)–(i) 750 nm, respectively.
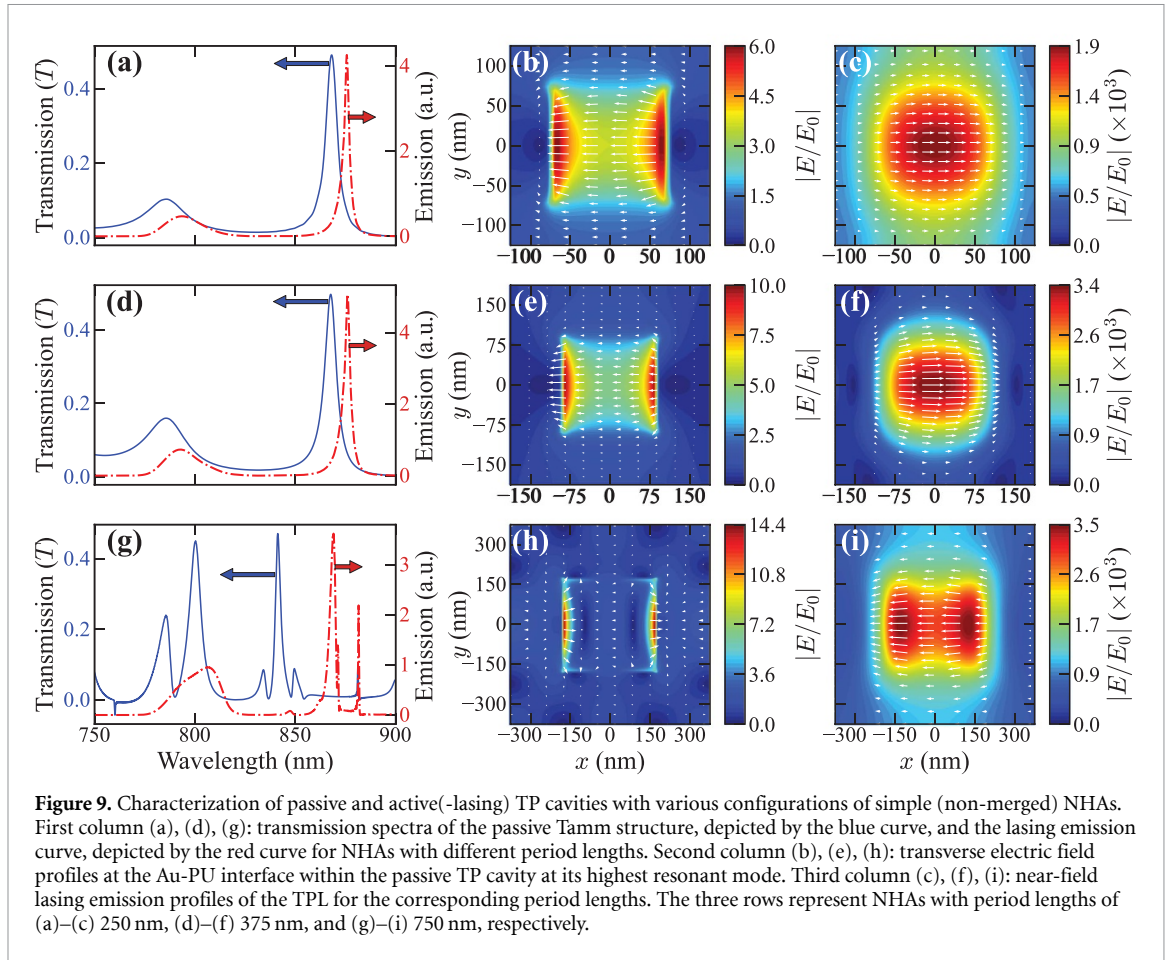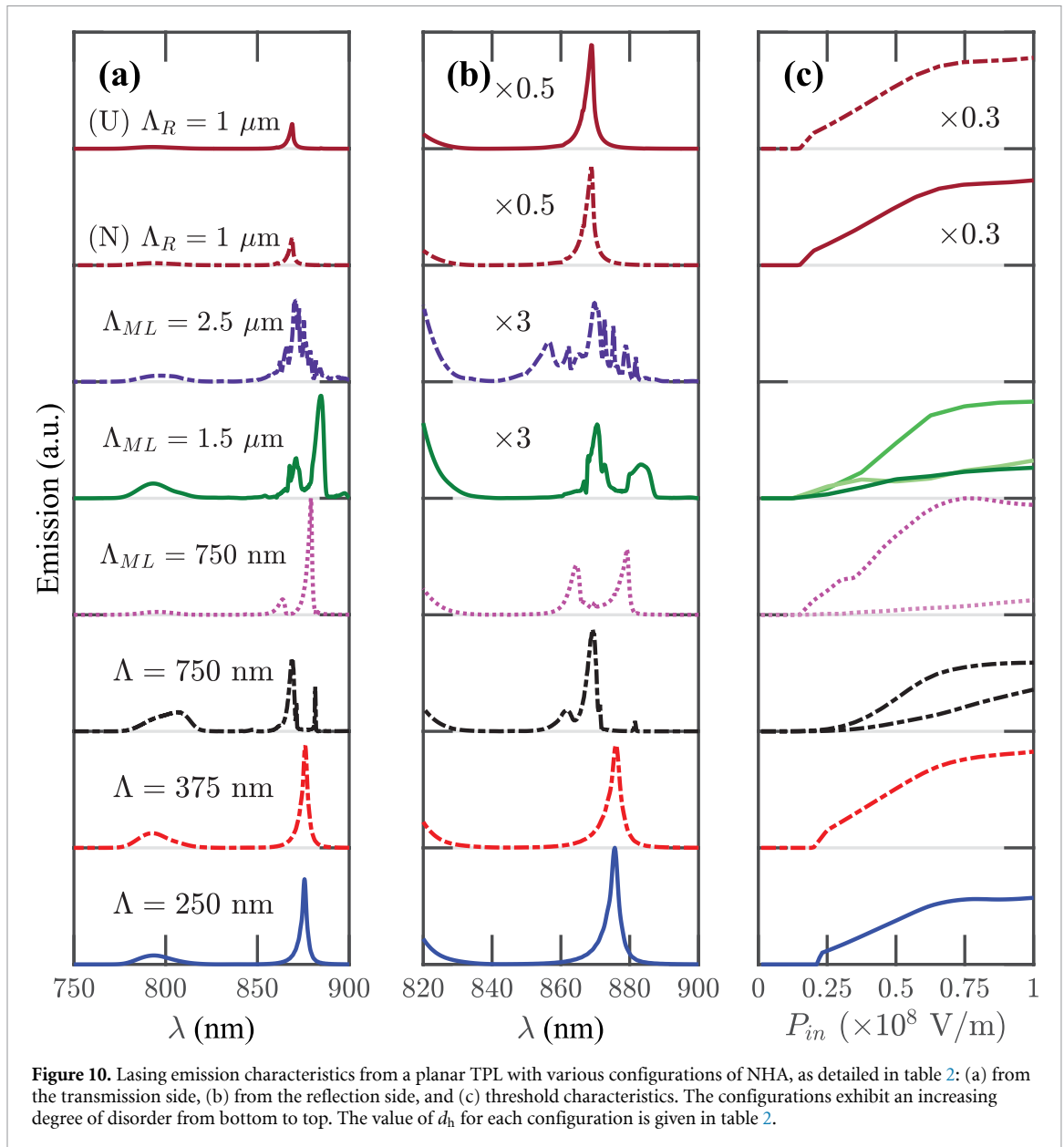
Table 2. List of optimized values of d_h for different laser configurations along with their respective pump thresholds P_{Th}.

NHA configurations		Optimized d_h (nm)	Threshold pump P_{Th} ($\times 10^7$ V m^{-1})
Λ	250 nm	143	2.12
	375 nm	175	2.01
	750 nm	350	2.70
Λ_{ML}	750 nm	143	1.50
	1.5 μm	175	1.21
	2.5 μm	175	—
Λ_R (Both)	1 μm	100	1.51

$\Lambda = 750$ nm. The $\Lambda = 750$ nm device exhibits visibly better plasmonic mode confinement at the hole edges. The difference in field enhancement between the passive devices is similarly observed between the transverse near-field profiles of the active devices. The $\Lambda = 750$ nm device exhibits a notable maximum field amplification of 3500, surpassing the 1900 times enhancement observed in the $\Lambda = 250$ nm device.

The lasing cavity formed by the TP structure supports modes in the 860–890 nm wavelength range. Dual modes can be achieved with appropriate Au-NHA patterning, as shown in figure 9(g). IR-140 dye molecules provide gain to these cavity modes. To observe the lasing characteristics of our structure, lasing at both the transmission and reflection ends of the device was evaluated. The lasing spectrum and the laser's input vs. output characteristics are summarized in figure 10. Figures 10(a) and (b) show the transmission and reflection side lasing spectra, respectively, while figure 10(c) displays the threshold characteristics, with input vs. output characteristics.

We simulated seven NHA lattice configurations on the Au film. The first three rows in figure 10, starting from the bottom, are from simple NHA patterned TPLs. The lasing spectra and emission transfer characteristics for $\Lambda = 250$ and 375 nm are almost similar, with single mode emission and only slight differences between their emission intensities. We observe dual mode emissions for the simple NHA's 750 nm

Figure 10. Lasing emission characteristics from a planar TPL with various configurations of NHA, as detailed in table 2: (a) from the transmission side, (b) from the reflection side, and (c) threshold characteristics. The configurations exhibit an increasing degree of disorder from bottom to top. The value of d_h for each configuration is given in table 2.

unit cell. The threshold characteristics in this configuration are slightly different from those mentioned above in that the emission intensity shows a more gradual increase with increasing pump value rather than an abrupt rise. Even the threshold of the two lasing modes is also different, where the higher wavelength lasing mode shows an almost linear increase, as opposed to the abrupt increase of the higher wavelength lasing mode.

The fourth to sixth rows in the first and second columns are TPLs with ML NHA. The pink dotted and green solid curves show the results for $\Lambda_{ML} = 0.75$ and $1.5\,\mu m$, whereas the purple dashed line shows the characteristics of the $\Lambda_{ML} = 2.5\,\mu m$ configuration. In contrast to the consistent narrowband emission of the simple NHAs, the lasing modes in the ML configuration exhibit broadening as Λ_{ML} increases. Multimode emission is also noticeable. Despite a highly asymmetrical dual-mode emission, the $\Lambda_{ML} = 750\,nm$ device shows the highest emission from the transmission side among the analyzed NHA configurations. By tuning d_h in that particular configuration, the emission via the two modes may be equal at the cost of the emission intensity. For configurations with $\Lambda_{ML} = 1.5$ and $2.5\,\mu m$, the modes are significantly broadened, with the latter showing the greatest broadband emission centered at 870 nm.

Additionally, the emissions from the reflection side are significantly reduced, almost three times lower than in previous configurations. As the laser with the ML hole configurations exhibits multiple modes, although broadened, their threshold characteristics are similar to the ones seen for the simple hole array configuration with multiple modes, i.e. $\Lambda = 750\,nm$. They both exhibit a phenomenon where the comparatively weaker mode gradually increases with the pump, almost linearly. In contrast, the dominant
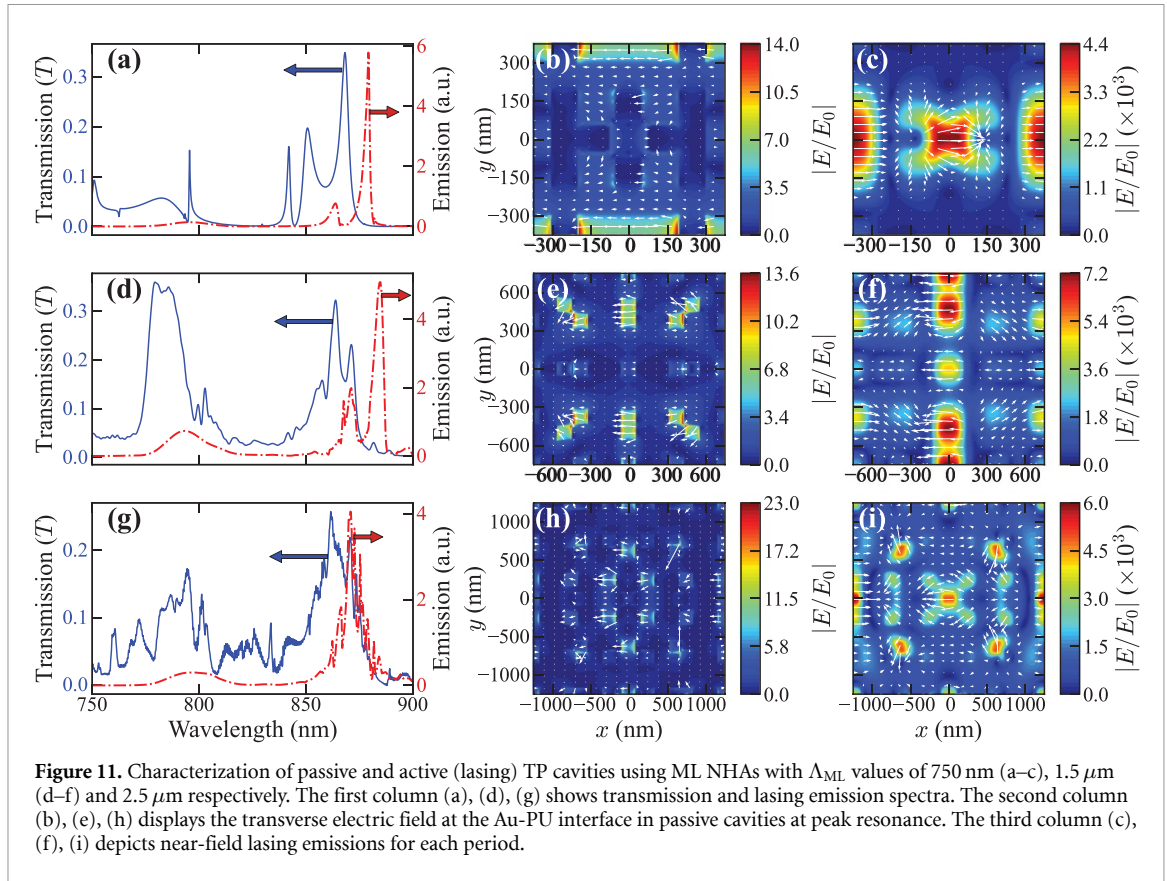
Figure 11. Characterization of passive and active (lasing) TP cavities using ML NHAs with Λ_{ML} values of 750 nm (a–c), 1.5 μm (d–f) and 2.5 μm respectively. The first column (a), (d), (g) shows transmission and lasing emission spectra. The second column (b), (e), (h) displays the transverse electric field at the Au-PU interface in passive cavities at peak resonance. The third column (c), (f), (i) depicts near-field lasing emissions for each period.
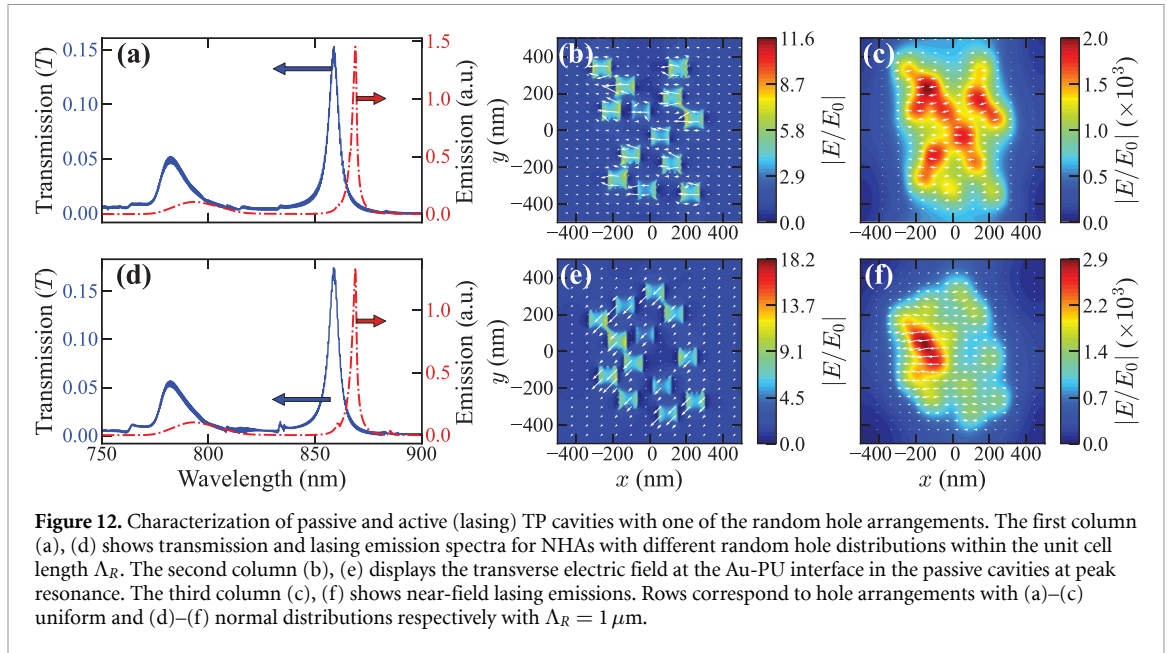
mode shows an abrupt increase in intensity right above the input pump threshold. Finally, the top two rows of figure 10 show results from a TPL with a random distribution of nanoholes on the metal layer, with a unit cell span of Λ_R. The emission from the transmission side of the device is greatly attenuated, compared to all the other non-random hole configurations, but high emission is observed from the reflection side.

The field profile and enhancement in the ML NHA configuration of the TP devices differ from those of their simple NHA counterparts. In the simple NHA configuration, the lasing modes exhibit comparable intensities, unlike the lasing modes of the ML configuration with unequal intensities. The blue transmission curve of the passive cavity with $\Lambda_{ML} = 750$ nm in figure 11(a) shows multiple transmission modes which result in two unequal lasing emission modes. Interestingly, the transmission resonances of the passive cavity with $\Lambda_{ML} = 1.5$ and 2.5 μm in figures 11(d) and (g) are much broader. The lasing modes in figures 11(d) and (g) are also broader compared to the lasing modes of the device with $\Lambda_{ML} = 750$ nm, let alone the devices with simple NHA. The field enhancement at the Au-PU interface of these passive ML configuration devices is at least comparable to or greater than the maximum field enhancement observed in the simple NHA devices. Furthermore, in figures 11(e) and (h), we find that field confinement and enhancement increase with higher values of Λ_{ML} with the $\Lambda_{ML} = 2.5\,\mu$m device displaying the best field confinement among the three ML configurations. We find that the field enhancement in all the configurations is maximized at the hole edges. In figure 9(f), the maximum lasing emission can be seen among all the classes of TPLs analyzed. This is exhibited by the ML configuration with $R = 4$ and $\Lambda_{ML} = 1.5\,\mu$m where the field is enhanced up to 7200 times.

3.3.1. Effect of randomness on lasing emission characteristics

The transmission spectrum of Au-NHA on the PU substrate shows a gradual split in the EOT resonance along with the emergence of new spectral modes as Λ or Λ_{ML} increases. Therefore, the increased period length leads to a greater density of modes. However, in the transition of the Au-NHA from Λ to Λ_{ML}, there is an increase not only in resonance splitting but also in flattening, but with a decrease in intensity of the EOT and TP modes. Flattening of modes near $k_x = 0$ means slower light and hence better confinement.

However, unlike ordered and ML NHA, the randomly placed holes in the metal film are not inherently good transmitters. When choosing a highly disordered array of holes, we find that the device no longer acts as a laser with high-intensity emission in the transmission regime. In such a case, the emission from the transmission side is weak and cannot produce a collimated beam because of the lack of coherence. Both uniform and normal distributions of randomly placed holes show similar single-mode emissions in

Figure 12. Characterization of passive and active (lasing) TP cavities with one of the random hole arrangements. The first column (a), (d) shows transmission and lasing emission spectra for NHAs with different random hole distributions within the unit cell length Λ_R. The second column (b), (e) displays the transverse electric field at the Au-PU interface in the passive cavities at peak resonance. The third column (c), (f) shows near-field lasing emissions. Rows correspond to hole arrangements with (a)–(c) uniform and (d)–(f) normal distributions respectively with $\Lambda_R = 1\,\mu$m.
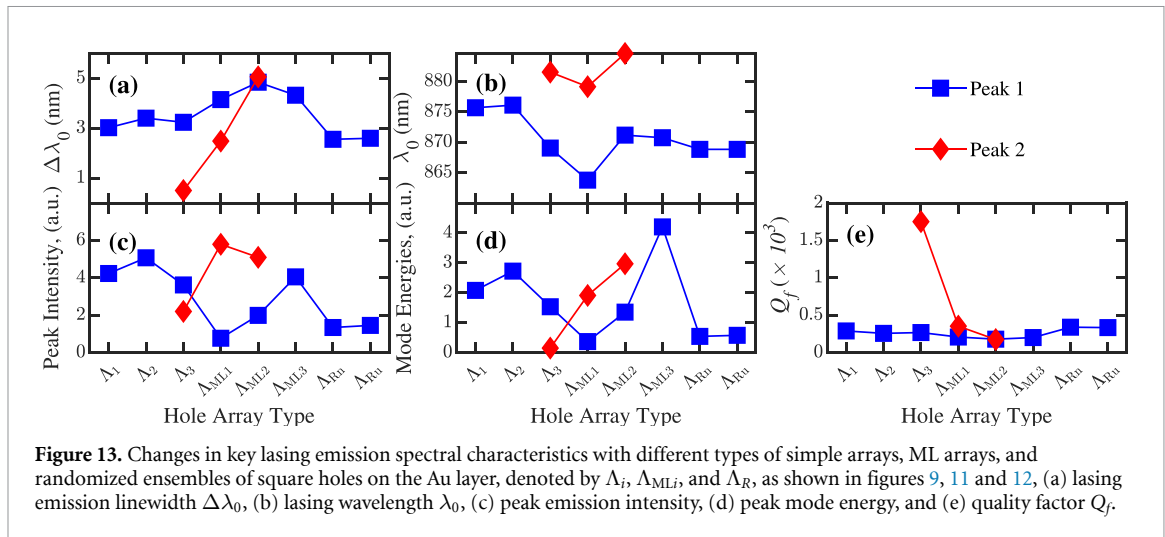
figures 10 and 12 arising from single resonances in the respective cavity transmission spectrum. From figure 12, it is clear that the type of randomness, i.e. uniform or normal distributions, does not show distinguishable differences in their resonance characteristics or near-field profiles.

The transmission spectrum of a TP cavity with randomly placed holes in the Au layer shows that the resonances converge to the unpatterned TP resonance at approximately 860 nm as $d_h \rightarrow 0$. This convergence occurs because the multiple resonances introduced by the holes within the $\Lambda_R \times \Lambda_R$ span randomly interfere, suppressing the emergence of distinct multiple resonant peaks. In contrast, the ML and simple periodic array configurations exhibit multiple resonant peaks in the transmission spectrum, influenced by the unit cell length and varying slightly with d_h, as shown in figure 7. However, in the random configuration, the incoherence resulting from the random positioning of the holes prevents the sustained emergence of other resonances. Consequently, the TPL with random holes only supports the primary TP resonance, which remains coherent, while other modes fail to achieve coherence and stability. As with all TPL devices, the electric field is maximized at the edges of the holes; however, the lasing emission's near-field profile is no longer symmetric due to the random positioning of the holes on the Au film.

The characteristics of the lasing emission, including linewidths, quality factors, peak intensities, and mode energies for various configurations, are summarized in figure 13. The first three simple hole array configurations, listed in the first three rows of table 2, are designated in figure 13 as Λ_i, where $i = 1, 2$, and 3 correspond to $\Lambda = 250$, 375, and 750 nm, respectively. Similarly, the three configurations of the ML array in the next three rows of table 2 are referred to as $\Lambda_{\mathrm{ML}i}$, with $i = 1, 2$, and 3 indicating $\Lambda_{\mathrm{ML}} = 0.75$, 1.5, and 2.5 μm, respectively. Additionally, the two random configurations of the nanoholes are labeled Λ_{Rn} and Λ_{Ru} for the normal and uniform random distributions of nanoholes, respectively. Our findings indicate that lasing emission displays two peaks only for the configurations Λ_3, Λ_{ML1}, and Λ_{ML2}. In contrast, all other configurations exhibit single-mode lasing emissions.

The emission linewidth is the broadest for the ML configurations, whereas the simple arrays exhibit relatively narrowband emissions. Notably, only the second peak of the Λ_3 configuration has a very sharp linewidth, resulting in an extremely high Q-factor for this peak. However, despite its sharpness, the intensity of this peak is not significant, as illustrated in figure 13(c). The simple array configurations, Λ_1, Λ_2, and Λ_3, demonstrate moderate lasing emissions. In contrast, the ML configuration shows the lasing emergence of multiple peaks, with Λ_{ML3} displaying emission modes that are nearly indistinguishable from the broadband lasing mode of the laser. Additionally, the energy associated with this mode, as shown in figure 13(d), is the highest. The quality factors in figure 13(e) remain relatively constant at ~400, except for the very narrow second peak in the Λ_{ML3} configuration, as illustrated in figures 9 and 10.

Therefore, whether we require a multimode or broadband lasing emission or strictly single mode emission will define our optimization goal alongside the trade-off associated with the design complexity involved in building the ML pattern. Furthermore, we can refer to the threshold behavior changes outlined in table 2 to support our design decisions. Based on our analysis, the best option is $\Lambda_{\mathrm{ML}} = 750$ nm, as it offers lower design complexity compared to other ML configurations while still achieving significant lasing at high

Figure 13. Changes in key lasing emission spectral characteristics with different types of simple arrays, ML arrays, and randomized ensembles of square holes on the Au layer, denoted by Λ_i, $\Lambda_{\text{ML}i}$, and Λ_R, as shown in figures 9, 11 and 12, (a) lasing emission linewidth $\Delta\lambda_0$, (b) lasing wavelength λ_0, (c) peak emission intensity, (d) peak mode energy, and (e) quality factor Q_f.

intensity. Lastly, in the periodically random regime, the lack of spatial coherence, as shown in figure 12, weakens the lasing emission.

3.4. Experimental and fabrication considerations

The design choices discussed in this paper focus on the arrangement of nanoholes within the topmost metal layer of a TPL cavity. Achieving ideal randomness in this context is challenging, and completely random designs can only be approximated within a tolerable margin of error. To address this issue, we have proposed a controlled method for introducing randomness into the 2D arrangement of nanoholes in the metal layer of the TP cavity. We explore randomness or disorder discretely using three types of hole arrangements, as described in section 2.1. Each of these three configurations includes some form of repeating unit cell, allowing for relatively simple fabrication of templates by maintaining a fixed periodicity in two dimensions. For instance, in the ML configuration, multiple templates with varying period lengths can be utilized, aligned according to equation (1).

In the third configuration, which features a pseudo-periodic random hole arrangement, the unit cell was set to $\Lambda_R = 1\,\mu\text{m}$ to ensure manageable simulation times. However, in experimental designs, Λ_R can be increased to meet practical fabrication constraints. The uniformly or normally distributed hole positions used in theoretical calculations can then be mapped and aligned onto a physical template for nanohole etching. Once the templates are created, the nanoholes can be etched into the metal layer using focused ion beam (FIB) milling or template stripping on an appropriate substrate [6, 52–54]. Although the FIB technique provides adequate results, template stripping is preferred to achieve finer resolution and smoother metal patterns.

The fabricated NHAs and the corresponding TP cavities with different hole arrangements can be characterized through transmission spectroscopy measurements [31, 55]. For lasing measurements, the TP structure can be illuminated by a suitable laser source at 800 nm. For such applications, it is common to use a mode-locked Ti:sapphire laser with a regenerative amplifier (800 nm wavelength, 1 kHz repetition rate, 40 fs pulse width) [41, 43]. The emitted laser beams can be captured and analyzed with a charge-coupled device. Further analysis and post-processing of the experimental data can be performed to extract energy distributions from the spectral measurements. These proposed steps and the general framework outlined in the previous sections can guide experimentalists in designing and fabricating nanostructures for tailored multimodal plasmonic lasing.

4. Conclusion

In conclusion, we conducted an in-depth analysis of the TP modes with various NHA configurations in multimodal plasmonic lasing. Our investigation focused on the impact of hole arrangements, examining both the dispersion and transmission characteristics of standalone metal films with NHAs, as well as the complete TPL devices. We demonstrated that different hole arrangement schemes can produce distinct types of TP modes, resulting in variations in plasmonic lasing. We explored the entire spectrum of nanohole arrangements, ranging from perfectly ordered arrays to completely disordered sets of holes, in relation to TPLs. We observe that the single-mode response of a regular periodic NHA evolves into a dual or multimodal response with the introduction of the ML configuration. While dual-mode lasing emerges for a

particular ML hole arrangement, other ML configurations show both dual and multimodal emissions, sometimes achieving nearly broadband lasing in TPLs. As the ML configuration incorporates elements of randomness, we also analyzed the role of randomness in the emergence of multiple modes. Our results suggest that an intermediate level of randomness, as observed in the ML configuration, is conducive to the emergence of multiple modes. However, a completely random arrangement of holes tends to yield a strictly single-mode response, with significantly reduced emission.

Data availability statement

The data cannot be made publicly available upon publication because they are not available in a format that is sufficiently accessible or reusable by other researchers. The data that support the findings of this study are available upon reasonable request from the authors.

Conflicts of interest

The authors declare no conflicts of interest.

ORCID iDs

Shadman Shahid ⬤ https://orcid.org/0000-0002-3103-9069
Muhammad Anisuzzaman Talukder ⬤ https://orcid.org/0000-0002-2814-3658

References

[1] Ebbesen T W, Lezec H J, Ghaemi H F, Thio T and Wolff P A 1998 Extraordinary optical transmission through sub-wavelength hole arrays *Nature* **391** 667–9
[2] Koerkamp K J K, Enoch S, Segerink F B, van Hulst N F and Kuipers L 2004 Strong Influence of Hole Shape on Extraordinary Transmission through Periodic Arrays of Subwavelength Holes *Phys. Rev. Lett.* **92** 183901
[3] van der Molen K L, Koerkamp K J K, Enoch S, Segerink F B, van Hulst N F and Kuipers L 2005 Role of shape and localized resonances in extraordinary transmission through periodic arrays of subwavelength holes: experiment and theory *Phys. Rev.* B **72** 045421
[4] Genet C and Ebbesen T W 2007 Light in tiny holes *Nature* **445** 39–46
[5] Giannattasio A, Hooper I R and Barnes W L 2004 Transmission of light through thin silver films via surface plasmon-polaritons *Opt. Express* **12** 5881
[6] Melentiev P N, Afanasiev A E, Kuzin A A, Zablotskiy A V, Baturin A S and Balykin V I 2011 Single nanohole and photonic crystal: wavelength selective enhanced transmission of light *Opt. Express* **19** 22743
[7] Treshin I V, Klimov V V, Melentiev P N and Balykin V I 2013 Optical Tamm state and extraordinary light transmission through a nanoaperture *Phys. Rev.* A **88** 023832
[8] Kavokin A V, Shelykh I A and Malpuech G 2005 Lossless interface modes at the boundary between two periodic dielectric structures *Phys. Rev.* B **72** 233102
[9] Kaliteevski M, Iorsh I, Brand S, Abram R A, Chamberlain J M, Kavokin A V and Shelykh I A 2007 Tamm plasmon-polaritons: possible electromagnetic states at the interface of a metal and a dielectric Bragg mirror *Phys. Rev.* B **76** 165415
[10] Martín-Moreno L, García-Vidal F J, Lezec H J, Pellerin K M, Thio T, Pendry J B and Ebbesen T W 2001 Theory of extraordinary optical transmission through subwavelength hole arrays *Phys. Rev. Lett.* **86** 1114–7
[11] Degiron A and Ebbesen T W 2005 The role of localized surface plasmon modes in the enhanced transmission of periodic subwavelength apertures *J. Opt. A: Pure Appl. Opt.* **7** S90–S96
[12] Liu H and Lalanne P 2008 Microscopic theory of the extraordinary optical transmission *Nature* **452** 728–31
[13] Krishnan A, Thio T, Kim T, Lezec H, Ebbesen T, Wolff P, Pendry J, Martin-Moreno L and Garcia-Vidal F 2001 Evanescently coupled resonance in surface plasmon enhanced transmission *Opt. Commun.* **200** 1–7
[14] Symonds C, Azzini S, Lheureux G, Piednoir A, Benoit J M, Lemaitre A, Senellart P and Bellessa J 2017 High quality factor confined Tamm modes *Sci. Rep.* **7** 3859
[15] Gazzano O, d. Vasconcellos S M, Gauthron K, Symonds C, Bloch J, Voisin P, Bellessa J, Lemaître A and Senellart P 2011 Evidence for confined Tamm plasmon modes under metallic microdisks and application to the control of spontaneous optical emission *Phys. Rev. Lett.* **107** 247402
[16] Symonds C, Lheureux G, Hugonin J P, Greffet J J, Laverdant J, Brucoli G, Lemaitre A, Senellart P and Bellessa J 2013 Confined Tamm plasmon lasers *Nano Lett.* **13** 3179–84
[17] Wang B, Yu P, Wang W, Zhang X, Kuo H, Xu H and Wang Z M 2021 High Q plasmonic resonances: fundamentals and applications *Adv. Opt. Mater.* **9** 2001520
[18] Konov Y V, Pykhtin D A, Bikbaev R G and Timofeev I V 2024 Tamm plasmon polariton-based planar hot-electron photodetector for the near-infrared region *Nanoscale* **16** 9570–5
[19] Poddar K, Sinha R, Jana B, Chatterjee S, Mukherjee R, Ranjan Maity A, Kumar S and Sona Maji P 2023 Exploring the potential of broadband Tamm plasmon resonance for enhanced photodetection *Appl. Opt.* **62** 8190–8190
[20] Zhong Y, Huang Y, Zhong S, Lin T, Zhang Z, Zeng Q, Yao L, Yu Y and Peng Z 2022 Tamm plasmon polaritons induced active terahertz ultra-narrowband absorbing with MoS$_2$ *Opt. Laser Technol.* **156** 108581
[21] Wu F and Xiao S 2023 Wide-angle high-efficiency absorption of graphene empowered by an angle-insensitive Tamm plasmon polariton *Opt. Express* **31** 5722–35
[22] Wu F, Wu X, Xiao S, Liu G and Li H 2021 Broadband wide-angle multilayer absorber based on a broadband omnidirectional optical Tamm state *Opt. Express* **29** 23976–87

[23] Bikbaev R G, Pykhtin D A, Vetrov S Y, Timofeev I V and Shabanov V F 2022 Nanostructured photosensitive layer for Tamm-plasmon-polariton-based organic solar cells *Appl. Opt.* **61** 5049–54

[24] Sharma A K, Srivastava A K, Maji P S and Kumar S 2024 Design of simultaneous refractive index sensor across multi-photonic bandgaps using Tamm plasmon modes *Plasmonics* **20** 1–11

[25] Chen Y-S, Yang Z-Y, Ye M-J, Wu W-H, Chen L-H, Shen H-J, Ishii S, Nagao T and Chen K-P 2023 Tamm plasmon polaritons hydrogen sensors *Adv. Phys. Res.* **2** 2200094

[26] Ahmed Z and Talukder M A 2018 An efficient and directional optical Tamm state assisted plasmonic nanolaser with broad tuning range *J. Phys. Commun.* **2** 045016

[27] Ahamed M, Afroj M N, Shahid S, Shahid S and Talukder M A 2024 Wavelength selective beam-steering in a dual-mode multi-layer plasmonic laser *Opt. Express* **32** 19895–909

[28] Shahid S, Zumrat S E and Talukder M A 2021 Merged lattice metal nanohole array based dual-mode plasmonic laser with ultra-low threshold *Nanoscale Adv.* **4** 801–813

[29] Xu W-H *et al* 2022 Tamm plasmon-polariton ultraviolet lasers *Adv. Photonics Res.* **3** 2100120

[30] Wang L and Jiang Y 2018 Confined dual hybrid states through coupling tamm plasmon and localized lattice resonance 10824

[31] Ferrier L, Nguyen H S, Jamois C, Berguiga L, Symonds C, Bellessa J and Benyattou T 2019 Tamm plasmon photonic crystals: from bandgap engineering to defect cavity *APL Photonics* **4** 106101

[32] Gubaydullin A R, Morozov K M and Kaliteevski M A 2020 Tamm plasmons in structures with quasiperiodic metal gratings *JETP Lett.* **111** 639–42

[33] Buchnev O, Belosludtsev A and Fedotov V 2022 Observation of a high-energy tamm plasmon state in the near-IR region *ACS Appl. Mater. Interfaces* **14** 13638–44

[34] Li N, Zou Q, Zhao B, Min C, Yuan X, Somekh M and Feng F 2023 Near-field manipulation of Tamm plasmon polaritons *Opt. Express* **31** 7321

[35] Zhu Y, Ma R, Dong A, Xu H, Wang C, Qin M, Liu J and Li H 2024 Tailoring second harmonic generation via strong coupling in a one-dimensional photonic crystal heterostructure *Adv. Photonics Res.* **n/a** 2400167

[36] Keene D and Durach M 2015 Hyperbolic resonances of metasurface cavities *Opt. Express* **23** 18577–88

[37] Azad Z, Islam M S and Talukder M A 2021 Mode-resolved analysis of a planar multi-layer plasmonic nanolaser *Opt. Commun.* **482** 126614

[38] Zumrat S-E-Z, Shahid S and Talukder M A 2022 Dual-wavelength hybrid tamm plasmonic laser *Opt. Express* **30** 25234–48

[39] Alagappan G and Png C E 2016 Localization of waves in merged lattices *Sci. Rep.* **6** 31620

[40] 2024 Ansys Lumerical FDTD | Simulation for Photonic Components (available at: www.ansys.com/products/optics/fdtd)

[41] Zhou W, Dridi M, Suh J Y, Kim C H, Co D T, Wasielewski M R, Schatz G C and Odom T W 2013 Lasing action in strongly coupled plasmonic nanocavity arrays *Nat. Nanotechnol.* **8** 506–11

[42] Johnson P B and Christy R W 1972 Optical constants of the noble metals *Phys. Rev.* B **6** 4370–9

[43] Yang A, Hoang T B, Dridi M, Deeb C, Mikkelsen M H, Schatz G C and Odom T W 2015 Real-time tunable lasing from plasmonic nanocavity arrays *Nat. Commun.* **6** 1–7

[44] Dastmalchi B, Tassin P, Koschny T and Soukoulis C M 2016 A New perspective on plasmonics: confinement and propagation length of surface plasmons for different materials and geometries *Adv. Opt. Mater.* **4** 177–84

[45] Baburin A S, Kalmykov A S, Kirtaev R V, Negrov D V, Moskalev D O, Ryzhikov I A, Melentiev P N, Rodionov I A and Balykin V I 2018 Toward a theoretically limited SPP propagation length above two hundred microns on an ultra-smooth silver surface *Opt. Mater. Express* **8** 3254

[46] Chang S-H and Taflove A 2004 Finite-difference time-domain model of lasing action in a four-level two-electron atomic system *Opt. Express* **12** 3827

[47] van der Molen K, Segerink F B, van Hulst N F and Kuipers L 2004 Influence of hole size on the extraordinary transmission through subwavelength hole arrays *Appl. Phys. Lett.* **85** 4316–8

[48] Maier S A 2007 *Plasmonics: Fundamentals and Applications* (Springer)

[49] Coe J V, Heer J M, Teeters-Kennedy S, Tian H and Rodriguez K R 2008 Extraordinary transmission of metal films with arrays of subwavelength holes *Annu. Rev. Phys. Chem.* **59** 179–202

[50] Ghaemi H F, Thio T, Grupp D E, Ebbesen T W and Lezec H J 1998 Surface plasmons enhance optical transmission through subwavelength holes *Phys. Rev.* B **58** 6779–82

[51] Schröter U and Heitmann D 1998 Surface-plasmon-enhanced transmission through metallic gratings *Phys. Rev.* B **58** 15419–21

[52] Adams D, Vasile M, Hodges C and Patterson N 2007 Focused ion beam fabrication of nanopores in metal and dielectric membranes *Microsc. Microanal.* **13** 1512–3

[53] Nagpal P, Lindquist N C, Oh S-H and Norris D J 2009 Ultrasmooth patterned metals for plasmonics and metamaterials *Science* **325** 594–7

[54] Winkler J M, Ruckriegel M J, Rojo H, Keitel R C, De Leo E, Rabouw F T and Norris D J 2020 Dual-wavelength lasing in quantum-dot plasmonic lattice lasers *ACS Nano* **14** 5223–32

[55] Le Thomas N, Houdré R, Kotlyar M V, O'Brien D and Krauss T F 2007 Exploring light propagating in photonic crystals with Fourier optics *J. Opt. Soc. Am.* B **24** 2964–71